JGR Space Physics

Key Points:

- Measurements of ionospheric vorticity enable the study of ionospheric turbulence
- Probability density functions (PDFs) of ionospheric vorticity are highly leptokurtic
- Modeling the PDFs of vorticity allows the estimation of the probability of extreme vorticity

A Statistical Model of Vorticity in the Polar Ionosphere and Implications for Extreme Values

G. Chisham[1] and **M. P. Freeman[1]**

[1]British Antarctic Survey, Cambridge, UK

Abstract Measurements of vorticity in the Earth's ionosphere enable the characterization of turbulent structure in the ionospheric plasma flow and how it varies spatially in relation to large-scale magnetic field-aligned current (FAC) systems. We have determined the spatial variation of the probability density function (PDF) of ionospheric vorticity measurements made by the Super Dual Auroral Radar Network (SuperDARN) across the northern polar ionosphere for the 6-year interval 2000–2005 inclusive. These PDFs are highly leptokurtic, with heavy tails, and are well-modeled by Tsallis q-exponential probability distributions. The parameters of the model q-exponential distributions have been determined using maximum likelihood estimation, resulting in a statistical model of ionospheric vorticity that covers the polar ionosphere. The spatial variation of the model parameters is highly variable, with the shape and scale of the model distributions varying systematically in relation to the well-known FAC regions, showing that FACs have a major influence on the character of ionospheric plasma vorticity. From the model distributions, we estimate the probability of observing extreme vorticity values with the SuperDARN radars (beyond thresholds of 5, 10, 20, and 40 mHz) across the northern polar ionosphere.

Plain Language Summary The term space weather defines the day-to-day variability of physical processes at the edges of the Earth's atmosphere and in the space environment. As with extreme meteorological weather in the lower atmosphere, it is important to understand the probability of occurrence of instances of extreme space weather. One way that this can be achieved is by using space weather observations to develop models of the probability of occurrence of space weather events of different intensity. Here, we specifically study the vorticity of the flow of ionized gases (plasma) in the Earth's ionosphere (located at an altitude of 250–400 km). Vorticity is a measure of how straight or curved this flow of plasma is at a given location, and its intensity is closely related to turbulence within the ionospheric environment. By making multiple measurements of vorticity across different locations in the high-latitude ionosphere, we can model the probability distributions of vorticity at a range of locations. The probability of observing extreme values of vorticity can then be estimated from these model distributions, allowing us to quantify the likelihood of extreme space weather.

1. Introduction

In the high-latitude F-region ionosphere, the large-scale behavior of plasma flow and how it responds to different driving conditions in the solar wind and magnetosphere is well understood (e.g., Cowley & Lockwood, 1992; Lockwood et al., 1990). However, flow characteristics on small and meso scales have yet to be fully explored and explained. As originally remarked by Dungey (1961), turbulence is a likely framework and now there is evidence that turbulence occurs in the high-latitude ionosphere from global (~1,000 km) to auroral arc (~10 km) scales (Abel et al., 2006, 2007, 2009; Chaston et al., 2008, 2010, 2011; Kintner & Seyler, 1985).

Turbulence can be modeled as the breakup of vortical eddies down to successively smaller scales; the largest eddies can be thought of as the two cells of the Dungey convection cycle (Abel et al., 2006). An important property of turbulence is intermittency, where the occurrence of extreme velocity and vorticity is much more likely than expected from a normal/Gaussian distribution. Intermittency arises by the unequal sharing of energy between eddies at each scale of the turbulent cascade (Anselmet et al., 2001). The resulting long-tailed non-Gaussian distributions are associated with the appearance in the velocity or vorticity field of both relatively quiet and extreme-valued regions (e.g., Boffetta et al., 2002; Pasquero & Falkovich, 2002; Wilczek & Friedrich, 2009). The relatively high frequency and unpredictability of extremes in intermittent

turbulence has significant consequences for forecasting the impact of space weather on space- and ground-based technological systems, such as the impact of geomagnetically induced currents (GICs) on power grids (Barbosa et al., 2017; Freeman et al., 2019).

In the aforementioned studies of Abel et al. (2006, 2007, 2009), it was suggested that the intermittency in the open geomagnetic field line region of the ionosphere is inherited from the turbulent solar wind to which it is magnetically connected. This is evidenced not only by a similar degree of intermittency in the ionosphere and solar wind (Abel et al., 2007), but also the fact that the intermittency disappears when the interplanetary magnetic field (IMF) is northward (Abel et al., 2009), and the flow on remnant open field lines is no longer directly driven by the solar wind (Lockwood et al., 1990). Outside the open field line region, Abel and colleagues did not measure intermittency directly but inferred it must be different, both because of the different physics expected in the closed field line auroral zones and because the first-order structure function differs from that in the open field line region and to that of a solar wind coupling function (Abel et al., 2006).

Further evidence for a spatial variation in ionospheric intermittency is provided by the non-Gaussian nature of flow vorticity (Chisham & Freeman, 2010). Measurements of vorticity in the natural environment are very limited due to the difficulties involved in making two- and three-dimensional flow measurements (e.g., Hughes et al., 2010; Sardeshmukh & Sura, 2009). However, in the ionosphere, vorticity can be measured using the Super Dual Auroral Radar Network (SuperDARN) (Chisham et al., 2009; Sofko et al., 1995). Here, vorticity in the plasma flow is associated with the magnetic field-aligned currents (FACs) that flow into and out of the ionosphere (Hasegawa & Sato, 1979; Vasyliunas, 1984), and which transfer energy and momentum between the magnetosphere and ionosphere (Cowley, 2000; Stern, 1983). This relationship has been explicitly demonstrated by the organization of the average ionospheric vorticity measured at fixed geomagnetic coordinates relative to the Earth-Sun line into clearly defined spatial regions (Chisham et al., 2009), corresponding to the so-called "region 0" (R0), "region 1" (R1), and "region 2" (R2) large-scale FAC systems (Erlandson et al., 1988; Iijima & Potemra, 1976a, 1976b). The average spatial pictures of ionospheric vorticity (Chisham et al., 2009) and FACs (Anderson et al., 2008; Edwards et al., 2020; Weimer, 2001, 2005) in the polar ionosphere and their large-scale variation with respect to changes in the IMF and season are well known. However, studies of the probability distributions of the fluctuations of these quantities and the physical reasons for the spatial variation of these distributions are in their infancy.

By analyzing millions of ionospheric F-region magnetic field-aligned vorticity measurements made by SuperDARN, Chisham and Freeman (2010) showed that the probability density function (PDF) of ionospheric vorticity is intermittent. Specifically, the PDF is leptokurtic (higher kurtosis than a Gaussian) at all locations throughout the high-latitude polar ionosphere and is most often heavy-tailed (higher kurtosis than an exponential). The shape and scale of measured PDFs can be described by the moments of the distributions (e.g., mean, variance, skewness, and kurtosis, etc.). However, the fitting of model distributions to the observed PDFs can provide more insight into their origins. It also allows the estimation of the probability of the occurrence of extreme values. Chisham and Freeman (2010) successfully modeled ionospheric vorticity PDFs using Tsallis q-exponential distributions (Picoli et al., 2009; Tsallis, 2009). In space plasmas, q-distributions have been used to characterize interstellar turbulence (Esquivel & Lazarian, 2010), turbulence in the solar wind (Burlaga et al., 2007), and geomagnetically induced currents (GICs) (Barbosa et al., 2017).

Here, we build on the study of Chisham and Freeman (2010) by analyzing the spatial variation of the shape and scale parameters of the q-exponential PDFs of vorticity fluctuations across the northern hemisphere polar ionosphere. We further use these model distributions to determine the probability of observing extreme values of vorticity in different regions of the high-latitude ionosphere. Section 2 outlines the methodologies used to determine vorticity from SuperDARN data, to compile the vorticity PDFs, to fit the model distributions to the PDFs, and to determine the probabilities of extreme values. Section 3 shows the results of the modeled PDF parameter variation across the northern polar ionosphere, and the estimates of the probabilities of extreme vorticity. Section 4 discusses the analysis and results. Section 5 summarizes the paper.
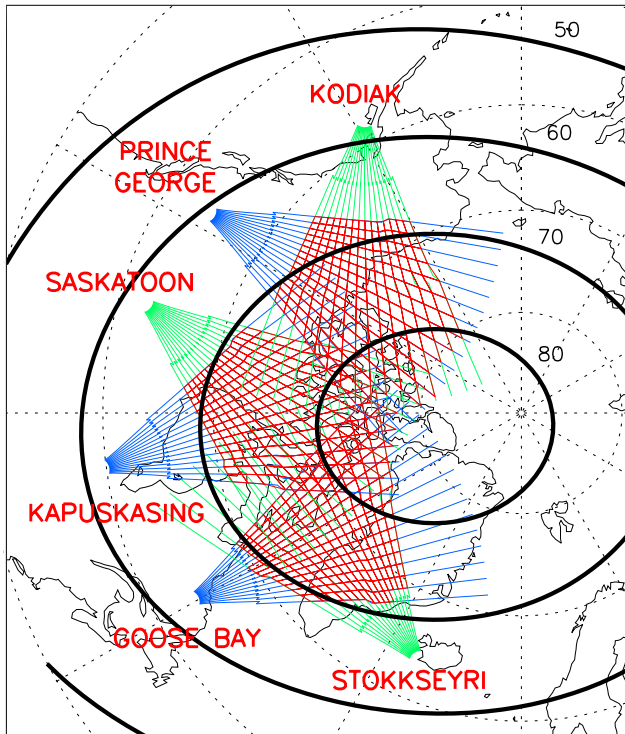
Figure 1. Map showing the fields of view of the six Super Dual Auroral Radar Network radars used in this study (Kodiak, Prince George, Saskatoon, Kapuskasing, Goose Bay, and Stokkseyri). The blue and green lines show the central look directions of the 16 beams used by each of the radars. The red lines highlight the region where the radar look directions overlap and define the closed measurement cells used in the vorticity estimation process. The dashed lines represent a geographic coordinate grid. The bold black lines represent Altitude-Adjusted Corrected GeoMagnetic latitude contours at 10° intervals.

2. Data Analysis Methodology

2.1. SuperDARN Vorticity Measurements

SuperDARN is a network of coherent scatter HF radars designed to measure large- and meso-scale plasma flow in the Northern and Southern polar and mid-latitude ionosphere (Chisham et al., 2007; Greenwald et al., 1995; Nishitani et al., 2019). Each radar in the network measures the line-of-sight component of the plasma velocity in the E- and F-region ionosphere over a 16- to 24-beam scan field of view (with beams typically separated by ~3.24° azimuth). Hence, the total field of view of each radar covers a spatial area of ~$5 \times 10^6 \, km^2$. The duration of a full scan of the field of view is typically 1 or 2 min.

Many of the SuperDARN radars are organized in pairs that have overlapping fields of view. Using the method presented by Chisham et al. (2009), it is possible to estimate the magnetic field-aligned vorticity of the ionospheric plasma flow across these overlapping fields of view. The method makes use of Stokes' theorem; determining localized measurements of vorticity by measuring the ionospheric plasma flow around closed loops defined by the geometry of the overlapping radar beams (see also Sofko et al., 1995).

Following the original study of Chisham et al. (2009), we have used vorticity measurements from three northern hemisphere SuperDARN radar pairs (Prince George/Kodiak, Saskatoon/Kapuskasing, and Goose Bay/Stokkseyri), from the 6-year interval 2000–2005 inclusive (Chisham, 2020). Figure 1 shows a map that indicates the overlapping fields of view of these radars on a geographic coordinate grid (dashed lines), overlaid with Altitude-Adjusted Corrected GeoMagnetic (AACGM) latitude contours at 10° intervals (bold lines). The look directions of the beams of each radar are shown as either blue lines (for Prince George, Kapuskasing, and Goose Bay) or green lines (for Kodiak, Saskatoon, and Stokkseyri), except where the radar fields of view overlap, where the beams are colored red, defining the closed loops discussed above. Hence, the red quadrilaterals in Figure 1 represent the vorticity measurement cells, and

the vorticity estimates in these cells are tagged to the coordinates at the center of these cells. The mapping of the fields of view uses the empirical virtual height model of Chisham et al. (2008) that has been shown to map far-range backscatter more accurately than the standard SuperDARN virtual height model (Yeoman et al., 2008).

The spatial resolution of the vorticity measurements varies across the field of view shown in Figure 1. The measurement cell area ranges in size from ~5,000 km^2, for the smallest cells at ranges nearest to the radars (lower latitudes), to ~50,000 km^2, for the largest cells at far ranges (higher latitudes). The typical cell size is ~10,000–20,000 km^2. Our analysis resulted in ~11 million ionospheric vorticity measurements made over a wide range of AACGM latitudes (~66°–85°) and over the complete 24 hr of magnetic local time (MLT).

As in Chisham et al. (2009), a positive field-aligned vorticity (clockwise rotation when looking in the direction of the magnetic field into the northern hemisphere ionosphere) is equivalent to a negative (upward) field-aligned current, whereas a negative field-aligned vorticity (anticlockwise rotation when looking in the direction of the magnetic field into the northern hemisphere ionosphere) is equivalent to a positive (downward) field-aligned current.

We sorted the measured vorticity values from all the 1- and 2-min SuperDARN common mode radar scans during the 6-year epoch into spatial bins based on where the center of the relevant measurement cell was located at the time of the measurement. These bins were chosen to be 1 hr of MLT by 1° of AACGM latitude
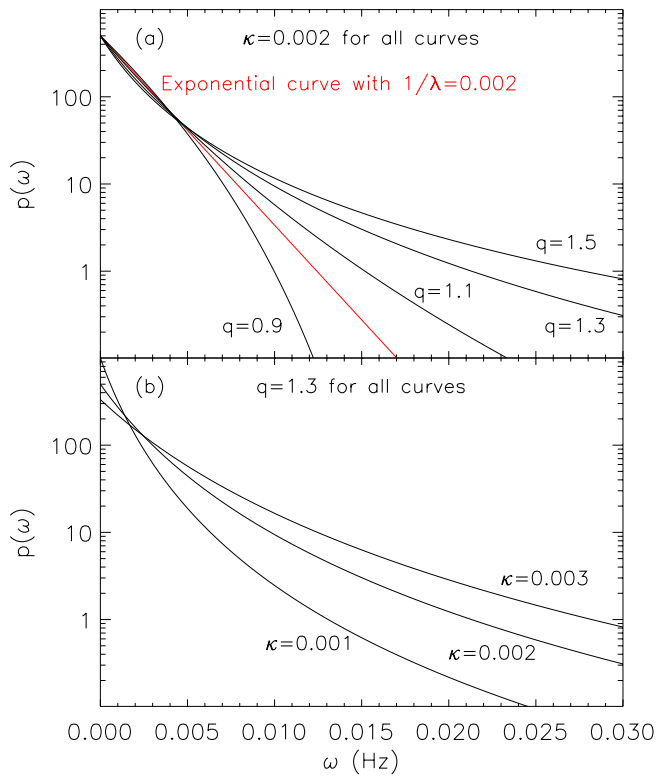
Figure 2. Example q-exponential model distributions for varying values of q and κ. (a) Curves for varying values of q (0.9, 1.0, 1.1, 1.3, and 1.5), with κ fixed to 0.002. The $q = 1$ curve is exponential and is highlighted by a red line. (b) Curves for varying values of κ (0.001, 0.002, and 0.003) with q fixed to 1.3.

as in Chisham et al. (2009). The vorticity values in each spatial bin were then used to compile the vorticity PDFs for the different spatial regions.

2.2. Modeling the Measured PDFs

In the preliminary work of Chisham and Freeman (2010), we used maximum likelihood estimation (MLE) to compare how well three different leptokurtic model distributions (exponential, Weibull, and q-exponential) could be fit to the observed PDFs at all locations. We considered the negative and positive vorticity measurements as separate distributions because the observed PDF variations for the different vorticity polarities were distinctly asymmetric and associated with oppositely directed FACs. Hence, for each vorticity distribution we considered two data sets, $\boldsymbol{\omega}_+ = \{\omega_1, \omega_2, \omega_3, \ldots, \omega_{n_+}\}$ comprised of n_+ elements for which $\omega_i > 0$ Hz and $\boldsymbol{\omega}_- = \{|\omega_1|, |\omega_2|, |\omega_3|, \ldots, |\omega_{n_-}|\}$ comprised of n_- elements for which $\omega_i < 0$ Hz (Here, ω represents the vorticity). We then identified the best fit of the potential model distributions to the positive and negative vorticity data sets at every spatial location. In that study, the q-exponential distribution provided the best fit at most locations. However, PDFs from parts of the dayside R1 were marginally better fitted by the Weibull distribution.

In this study, we have reconsidered this fitting methodology. First, because the measured PDFs are continuous through zero from the negative to positive measurements. This makes the Weibull an unsuitable model as Weibull distributions tend to either zero or infinity at a parameter value of zero, except in the limiting case where the Weibull tends to an exponential. Consequently, we only consider fitting the q-exponential to the measured PDFs in this paper. Second, when viewing the observed PDFs as they approach zero at higher resolution, it is clear that the modes of the distributions are typically shifted slightly away from zero. Hence, dividing the PDF fitting around zero vorticity is not an optimum approach. Consequently, we now consider our two data sets as those either side of the mode; $\boldsymbol{\omega}_+ = \{\omega_1 - \omega_m, \omega_2 - \omega_m, \omega_3 - \omega_m, \ldots, \omega_{n_+} - \omega_m\}$ comprised of n_+ elements for which $\omega_i > \omega_m$, where ω_m is the mode of the observed PDF and $\boldsymbol{\omega}_- = \{\omega_m - \omega_1, \omega_m - \omega_2, \omega_m - \omega_3, \ldots, \omega_m - \omega_{n_-}\}$ comprised of n_- elements for which $\omega_i < \omega_m$. Hence, we also determine ω_m across the whole polar region, similar to the determination of the mean value presented by Chisham et al. (2009).

We consider a q-exponential PDF of the form

$$f_{q,\kappa}(\omega) = \frac{1}{\kappa}\left(1 - \frac{(1-q)\omega}{\kappa}\right)^{q/(1-q)} \tag{1}$$

where the function tends to an exponential as $q \to 1$. The MLE parameters, $(\hat{q}_+, \hat{\kappa}_+)$ and $(\hat{q}_-, \hat{\kappa}_-)$, are determined from a numerical solution of the partial differentials of the log likelihood function for the q-exponential (Shalizi, 2007). We require $\boldsymbol{\omega}_+$ and $\boldsymbol{\omega}_-$ to be comprised of at least 100 elements each for an acceptable MLE output.

In Figure 2, we present example q-exponential distributions to illustrate how the distributions vary with the parameters q and κ (examples have been chosen to match the range of values typical of the measured ionospheric vorticity distributions). In panel a, the dimensionless shape parameter q is varied keeping the value of the scale parameter constant at $\kappa = 0.002$. The red curve represents the limiting case of the exponential $f(\omega) = (1/\kappa)\exp(-\omega/\kappa)$ that occurs when $q \to 1$ and which is a straight line on this log-linear plot. Larger values of q lead to distributions that are heavy-tailed whereas smaller values of q lead to distributions that are not heavy-tailed, but still leptokurtic. In panel b, the dimensional scale parameter κ is varied keeping a constant value of $q = 1.3$. Here, the mean of the distribution is proportional to κ, changing the scale of the distribution, but the shape of the distribution remains the same. The q-exponential distributions all tend

toward a power law for high values of ω, which is a subset of heavy-tailed distributions commonly referred to as fat-tailed.

2.3. Determining the Probability of Extreme Values

Once the model q-exponential parameters for the measured PDFs have been determined, it is possible to use the survival function to estimate the probability of extreme values of vorticity (both negative and positive). The survival function ($S(\omega)$) is the probability of observing a vorticity greater than, or equal to, ω. It is often called the complementary cumulative distribution function and is related to the cumulative distribution function (CDF, $F(\omega)$) by

$$S(\omega) = P(\Omega \geq \omega) = 1 - F(\omega) \tag{2}$$

where Ω is a continuous random variable representing the vorticity measurements. Hence, it is trivial to determine the survival function directly from the model q-exponential PDFs.

For the case of "positive" vorticity ($\omega > \omega_m$), the survival function can be written

$$P_{q_+, \kappa_+}(\Omega \geq \omega) = \frac{n_+}{n_+ + n_-}\left(1 - \frac{(1 - q_+)(\omega - \omega_m)}{\kappa_+}\right)^{1/(1-q_+)} \tag{3}$$

Similarly, for the case of "negative" vorticity ($\omega < \omega_m$), the survival function can be written

$$P_{q_-, \kappa_-}(\Omega \leq \omega) = \frac{n_-}{n_+ + n_-}\left(1 - \frac{(1 - q_-)(\omega_m - \omega)}{\kappa_-}\right)^{1/(1-q_-)} \tag{4}$$

3. Results

3.1. Example PDFs From Region 1 and Region 2

In this paper, the primary aim is to model the PDFs of vorticity measurements at all spatial locations in order to be able to estimate the probability of the occurrence of extreme vorticity and its spatial variation across the polar ionosphere. First, for illustrative purposes, we present example PDFs from the large-scale FAC regions. To select these regions, we look at the average vorticity variation across the polar ionosphere.

In Figure 3a , we reproduce the spatial distribution of mean vorticity measured by the three SuperDARN radar pairs, as originally presented in Figure 3 of Chisham et al. (2009). Here, the data are presented in the AACGM coordinate system, extending from 66° latitude to ~86° AACGM latitude. The vorticity value in each spatial bin (of size 1° AACGM latitude by 1 hr of MLT) was determined by averaging all the vorticity values measured in that bin location. The mean vorticity values were only presented for spatial bins where there were more than 100 measurements in that bin (see Chisham et al., 2009, for the occurrence distribution of vorticity values across all bins). As described in Chisham et al. (2009), the mean vorticity map shows clear features, which match those of the average picture of the distribution of large-scale R1 and R2 FAC systems observed in average FAC maps (Anderson et al., 2008; Edwards et al., 2020; Weimer, 2001, 2005). In order to highlight the main R1 and R2 current regions, in Figure 3b we replot the spatial variation of the mean vorticity, but filter out mean vorticity values that have magnitudes of less than 0.4 mHz (shown as white). This leaves four distinct regions that represent the mean vorticity variation associated with the morning and afternoon R1 and R2 FAC systems.

In Figure 4, we present vorticity PDFs that are typical of the R1 and R2 FAC regions. Figure 4a presents the vorticity PDF (black square symbols and error bars) determined for the red hatched region in the morning sector R1 as illustrated in Figure 3b (74°–78° AACGM latitude and 0700–0800 MLT). Figure 4b presents the vorticity PDF (black square symbols and error bars) determined for the red hatched region in the morning sector R2 as illustrated in Figure 3b (67°–70° AACGM latitude and 0600–0700 MLT). The PDFs are plotted on a log-linear scale, with a vorticity bin size of 1 mHz, to enable visualization of both the variations in the core and the tails of the PDFs.

The vorticity PDFs shown are all leptokurtic. This is the case for all the measured PDFs across the whole of the northern hemisphere polar ionosphere. The R2 PDFs in Figure 4 are more leptokurtic, with the R1
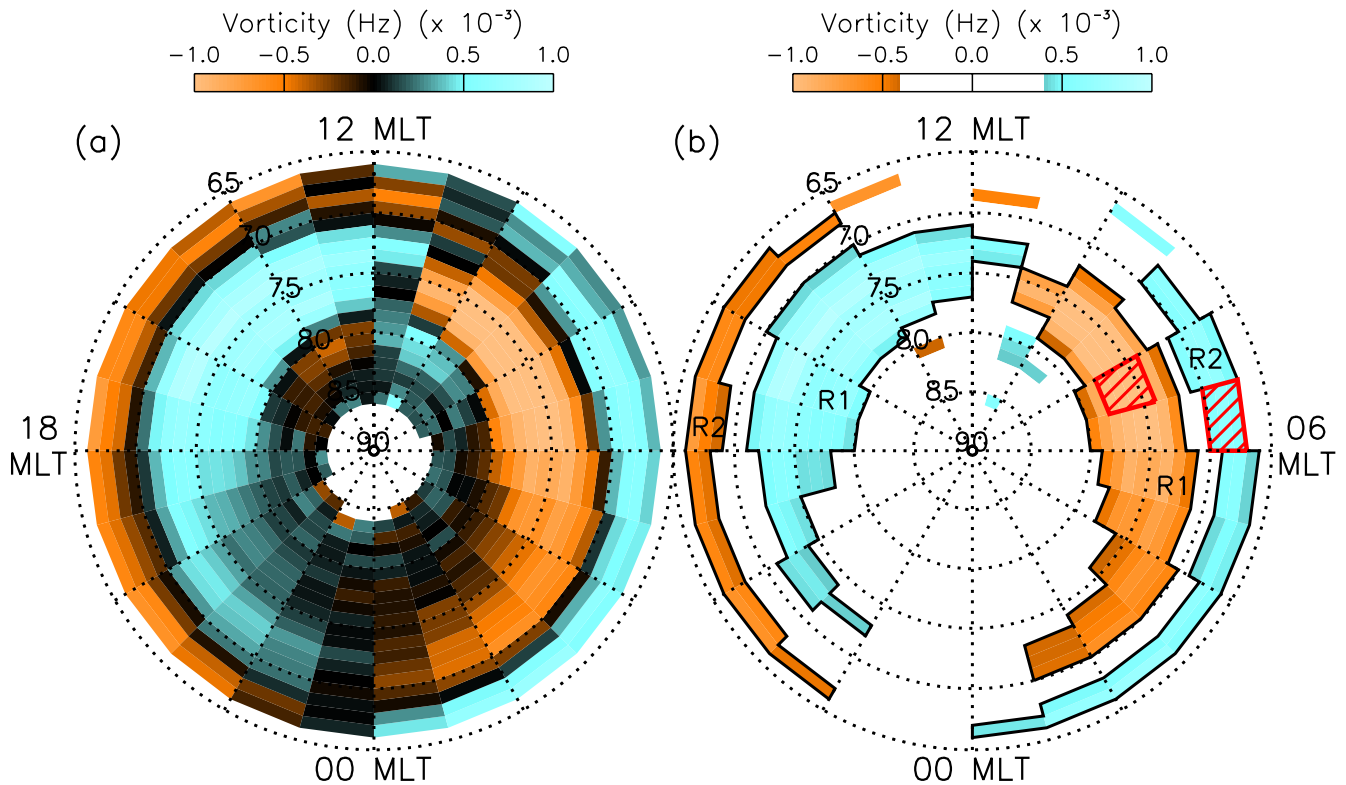
Figure 3. The spatial variation of mean vorticity across the northern polar ionosphere determined from measurements made over the years 2000–2005 inclusive (see text for details). (a) The mean vorticity values across the whole polar region, reproduced from Chisham et al. (2009). (b) The same data filtered to remove mean vorticity values with a magnitude of less than 0.4 mHz. The red hatched regions represent areas from where example distributions have been chosen for Figure 4.

PDFs being closer to exponential (i.e., closer to a straight line on the log-linear plot). The PDFs across the whole polar region are typically asymmetric showing that the character of the two senses of vorticity in any location are typically different. This is particularly clear in the R1 PDF in Figure 4a where the positive vorticity distribution is more leptokurtic than an exponential, whereas the negative vorticity distribution is less leptokurtic than an exponential. This asymmetry in the PDF shape is partially responsible for the variations seen in the spatial pattern of mean vorticity.

The MLE q-exponential fits to the measured PDFs are presented in Figure 4 as solid red lines. Inset in red text in Figure 4 are the MLE values of $\hat{q}$ and $\hat{\kappa}$ associated with the fitted curves. In both Figures 4a and 4b, the model curves appear to fit well to the observed PDFs over most of the range displayed. There are departures of the fits in the tails of the distributions, where the measurements approach the one count level and the statistics are poor. In Figure 4a, the values of $\hat{q}$ are close to 1.0 denoting that the R1 PDFs are reasonably close to exponential. In Figure 4b, the values of $\hat{q}$ are significantly higher than 1.0 denoting that the R2 PDFs are heavy-tailed.

The PDFs as shown in Figures 4a and 4b do not show the detailed behavior in the core of the distribution. In Figures 4c and 4d, we zoom in on the core of the PDFs shown in Figures 4a and 4b (specifically the gray-shaded regions in these figures from −4 to 4 mHz). To get a better view of the variation in the measured PDFs, we reduce the vorticity bin size to 0.2 mHz in Figures 4c and 4d. These figures now clearly show that the measured PDFs are continuous across zero, but that the PDF peaks are shifted from zero vorticity. The locations of the modes of the PDFs in Figures 4c and 4d are highlighted by the vertical red dotted lines. For comparison, the locations of the means of the PDFs are highlighted by the vertical orange dotted lines. The differences between the means and the modes provide information about how much of the mean value is a result of the offset of the distribution from zero and how much is a result of the asymmetry of the distribution about the mode. In Figure 4c (R1), the mode is very close to zero, but the significant asymmetry in the
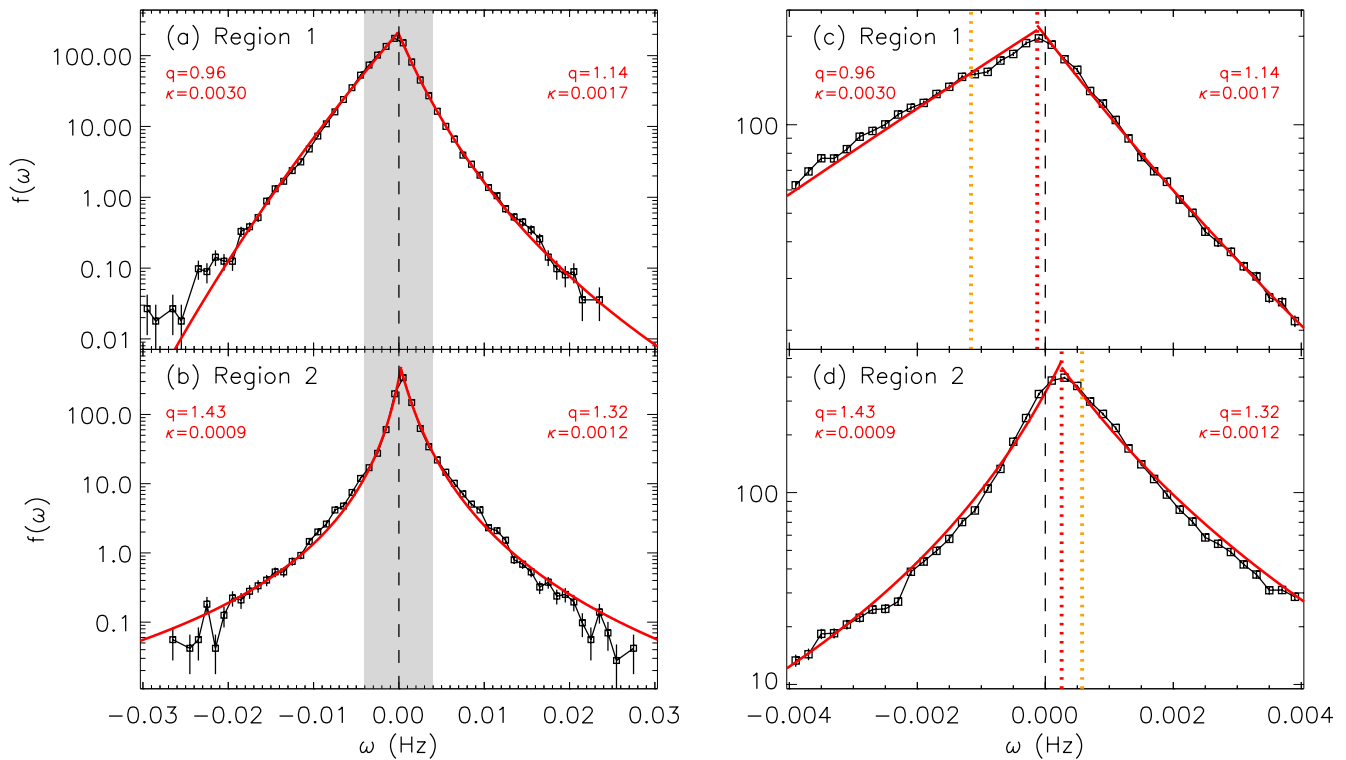
Figure 4. Example vorticity PDFs compiled from vorticity measurements made by the Super Dual Auroral Radar Network radars accompanied by q-exponential fits to the probability density functions (PDFs). (a) The black symbols and error bars show the PDF variation in a typical R1 field-aligned current (FAC) location (74°–78° Altitude-Adjusted Corrected GeoMagnetic [AACGM] latitude and 0700–0800 MLT). (b) The black symbols and error bars show the PDF variation in a typical R2 FAC location (67°–70° AACGM latitude and 0600–0700 MLT). In panels a and b, the vorticity bin size is 1 mHz. The solid red lines represent the q-exponential fits to the distribution, with the maximum likelihood estimation (MLE) fit parameters highlighted in red. The gray shaded region illustrates the vorticity range covered in panels c and d. (c) The black symbols and error bars show the PDF variation in the core of the typical R1 FAC location shown in panel a. (d) The black symbols and error bars show the PDF variation in the core of the typical R2 FAC location shown in panel b. In panels c and d, the vorticity bin size is 0.2 mHz. Again, the solid red lines represent the q-exponential fits to the distribution, with the MLE fit parameters highlighted in red. The vertical red dotted lines highlight the locations of the modes of the distributions. The vertical orange dotted lines highlight the locations of the means of the distributions.

PDF results in a much larger mean value. In Figure 4d (R2), the mode is further from zero than in the R1 case, but much closer to the mean, as the asymmetry in the PDF is reduced.

As in Figures 4a and 4b, the solid red lines show the MLE q-exponential fits to the PDF. Again, in both Figures 4c and 4d, the model curves provide good fits to the observed PDFs. At the very center of the distributions, close to the mode, the measured PDF is below the fit value. This is potentially the result of smoothing of the measured PDF due to vorticity measurement errors. We discuss the potential sources of measurement error later in the paper.

3.2. Spatial Variation of the Mode

Figure 5 presents the spatial variation of the mode of the vorticity PDFs across the northern hemisphere polar ionosphere, in a similar format to the mean variation presented in Figure 3a. Again, the data are presented in the AACGM co-ordinate system, extending from 66° latitude to ~86° latitude. The range of the vorticity scale has been reduced (from −0.4 to 0.4 mHz) compared to Figure 3, owing to the mode values being consistently lower than the mean values for all the PDFs.

As suggested by the example PDFs presented in Figures 4c and 4d, the relationship between the PDF modes and means is typically different in R1 to what it is in R2. In R1, the mode is typically between a magnitude of 0 and ~0.2 mHz, whereas the mean is typically ~1.0 mHz. Hence, it is the asymmetry in the PDFs (essentially the differences between the clockwise and counter-clockwise vorticity populations) that are
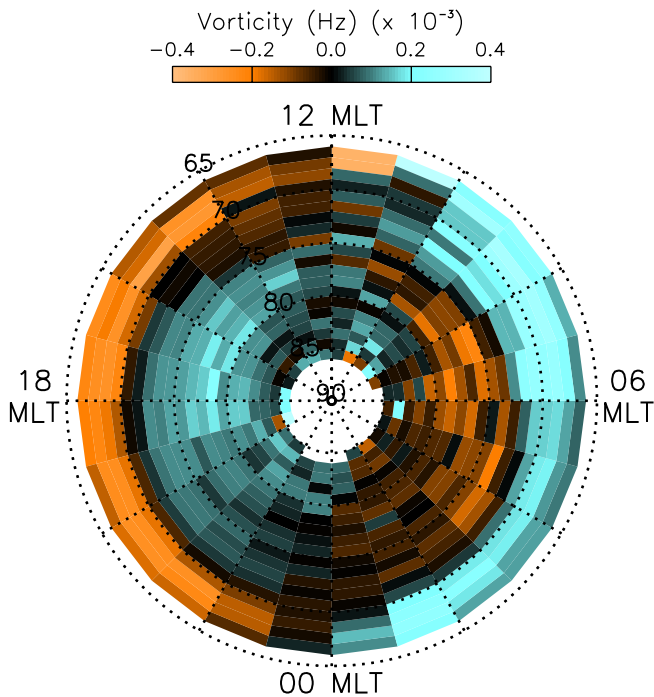
Figure 5. The spatial variation of the mode of the vorticity probability density function across the northern polar ionosphere determined from measurements made over the years 2000–2005 inclusive (see text for details).

predominantly responsible for determining the mean value. In R2, the mode is typically ~0.2 to ~0.4 mHz in magnitude compared to a mean value of ~0.5 to ~0.8 mHz. Here, the shift of the mode away from zero plays as big a role in the determination of the mean as any asymmetry in the PDF.

3.3. Spatial Variation of the q-Exponential Fit Parameters

The MLE analysis demonstrated in Figure 4 has been used to model the vorticity PDFs across the complete northern polar ionosphere, for the data in each 1° AACGM latitude by 1 hr of MLT bin. Figure 6 shows the spatial variation of the q-exponential MLE parameters $(\hat{q}, \hat{\kappa})$ determined by this analysis. Panels a and b of the figure show the parameters for the "positive" vorticity PDFs (relative to the mode; $\omega > \omega_m$), whereas panels c and d show those for the "negative" vorticity PDFs (relative to the mode; $\omega < \omega_m$).

The variations of $\hat{q}$ and $\hat{\kappa}$ across the northern hemisphere ionosphere vary significantly with region:

1. Region 2 (equatorward of ~70° AACGM latitude)—Here, the PDFs are characterized by high values of $\hat{q}$ (~1.3–1.8) and low values of $\hat{\kappa}$ (~0.001 or lower). Hence, the heavy-tailed R2 PDFs shown in Figures 4b and 4d are characteristic of the R2 PDFs.
2. Dayside Region 1 (between ~70° and ~80° AACGM latitude)—Here, the PDFs are typically characterized by low values of $\hat{q}$ (~0.9–1.1) and high values of $\hat{\kappa}$ (~0.002 to 0.004). Hence, these PDFs are very close to exponential, similar to those in Figures 4a and 4c. There is an obvious asymmetry in this region between the "positive" and "negative" vorticity results, with PDFs being more nearly exponential where the mean is of the same sign.
3. Nightside Region 1 (between ~70° and ~75° AACGM latitude)—Here, the PDFs are typically characterized by intermediate values of $\hat{q}$ (~1.1–1.4) and intermediate values of $\hat{\kappa}$ (~0.0015 to 0.0025). The same asymmetry seen in the Dayside R1 is apparent here too.
4. The Polar Cap (poleward of ~80° AACGM latitude on the dayside and poleward of ~75° AACGM latitude on the nightside)—Here, the PDFs are typically characterized by intermediate to high values of $\hat{q}$ (~1.2–1.5) and low values of $\hat{\kappa}$ (~0.001 or lower), similar to those seen at lower latitudes.

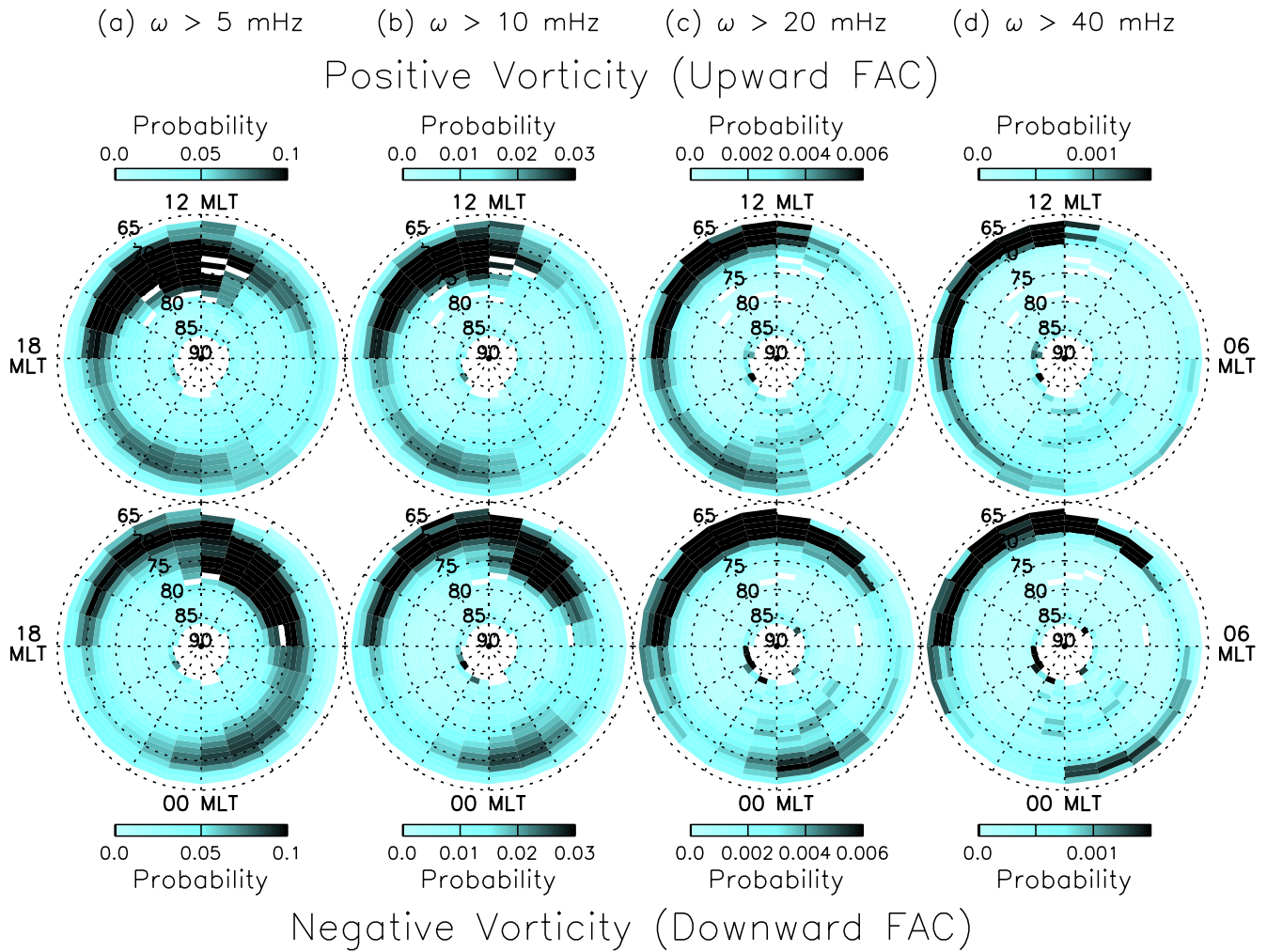### 3.4. Spatial Variation of the Probability of Extreme Values

Estimates of the values of both q and κ, in addition to the mode, ω_m, at any location, allow the reconstruction of the model vorticity PDF at that location. Hence, by using the q-exponential fit parameters from Figure 6, the mode from Figure 5, and the survival function Equations 3 and 4, we can determine the probability that the ionospheric vorticity on the spatial measurement scales allowed by the SuperDARN configuration will exceed any particular magnitude.

In Figure 7, we present examples of the spatial variation of this probability for four different thresholds of vorticity magnitude (5, 10, 20, and 40 mHz). Looking at Figures 4a and 4b suggests that 5 mHz is close to the edge of the core of the distribution. By 10 mHz, most PDFs have dropped to less than 1% of the peak value. By 20 mHz, the measured PDFs are typically very noisy due to poorer statistics, and so the q-exponential model fit most probably provides a better estimate of the true PDF at this point. The probability of identifying a vorticity above 40 mHz can only be estimated by an extrapolation of the q-exponential model fit as it is beyond the range of the measured values.

The higher probabilities for each threshold in Figure 7 (black) occur when the variance of the distributions is high. This is a combination of high values of q (which represent more leptokurtic distributions), and high
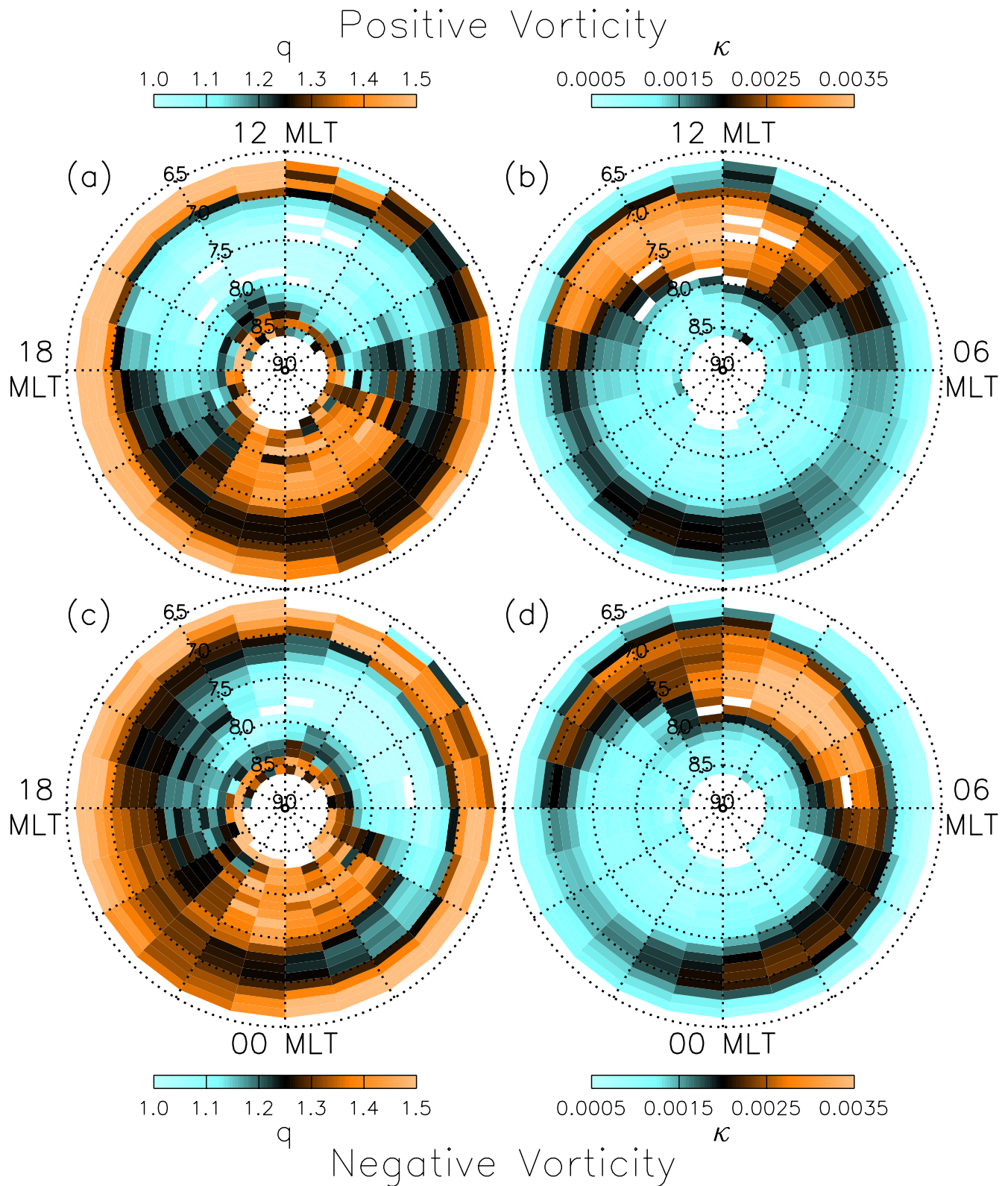
Figure 6. Spatial maps of the q-exponential maximum likelihood estimation fit parameters $\hat{q}$ (panels a and c) and $\hat{\kappa}$ (panels b and d) across the northern polar ionosphere for both positive (panels a and b) and negative (panels c and d) vorticity.

Figure 7. Spatial maps of the probability of extreme values of vorticity over different thresholds: (a) 5 mHz, (b) 10 mHz, (c) 20 mHz, and (d) 40 mHz. The top panel maps represent those for positive vorticity (equivalent to an upward field-aligned current [FAC]), whereas the bottom panel maps represent those for negative vorticity (equivalent to a downward FAC).

values of κ (which represent wider distributions). Interestingly, the regions of high q often coincide with the regions of low κ, and vice versa. This affects the extreme value probabilities in an interesting way. For the lower thresholds (5 and 10 mHz), the highest probabilities of vorticity above these thresholds occur in the dayside R1, characterized by low values of q, but high values of κ. Progressing toward the higher thresholds (20 and 40 mHz), the highest probabilities of the most extreme vorticity occur predominantly at lower latitudes in the dayside R2, characterized by high values of q, but low values of κ.

4. Discussion

4.1. Factors Affecting the Measured Vorticity PDFs

The physical processes driving ionospheric vorticity are the primary factors that determine the PDF of vorticity fluctuations. However, there are other factors associated solely with the measurement technique that affect the measured PDFs and consequently, the spatial variation of the PDF characteristics. These factors need to be fully appreciated in order to minimize the misinterpretation of the PDFs and their spatial variation. Here, we discuss the effects of some of these factors.

4.1.1. Mixture Distributions

It is likely that there are multiple processes that cause fluctuations in vorticity. These processes may occur at spatial locations that vary with time. Consequently, the distribution at a given location will be the mixture distribution of all processes that can create vorticity at that location.

The polar ionosphere is continually changing in response to variations in the energy input from the solar wind to the magnetosphere via magnetic reconnection, and the explosive release of energy from the magnetospheric system via substorms. The imbalance of these dayside and nightside reconnection processes results in the continual expansion and contraction of the open magnetic field line region within the polar cap (e.g., Cowley & Lockwood, 1992).

The location of the R1 FACs is intimately associated with the location of the polar cap boundary between the ionospheric footprints of open and closed magnetic field lines (Anderson et al., 2014; Clausen et al., 2012). Hence, the R1 and R2 current systems expand and contract in tandem with the motion of the polar cap boundary (Clausen et al., 2013; Coxon et al., 2014). If we assume that the R1 FAC systems are responsible for one type of vorticity distribution and that the R2 FAC systems are responsible for another type of vorticity distribution, then the motion of these current systems will result in a mixture distribution in the overlap region (where both R1 and R2 vorticities may both exist, at different times). This mixture distribution will be that sum of the R1 and R2 distributions weighted by their probability of occurrence at that location.

Hence, it is likely that some of the spatial variability in the estimated MLE parameters for vorticity distributions near boundaries between different FAC regions is a result of the temporal motion of these regions. Moving equatorward from the R1 peak (where the vorticity distribution may be purely R1), the probability of observing R1 vorticity would be expected to decrease, while that of R2 vorticity would be expected to increase, leading to mixture distributions. Moving further equatorward would result in the vorticity distributions tending toward purely R2 distributions. This might suggest that the "true" R1 and R2 distributions are those seen at ~74° and ~67°, respectively.

The adverse effect of the expanding and contracting polar cap on ionospheric climatologies and empirical models is a long standing problem. Combining measurements from the auroral zone and the polar cap has been known to blur sharp boundaries in empirical convection models (as discussed in Chisham, 2017). Similarly, auroral zone and sub-auroral measurements are often averaged together near the equatorward edge of the auroral oval. The observed data at fixed coordinates are generally a combination of measurements from the different spatial regions either side of these boundaries. In recent years, these problems have been addressed by the use of adaptive high-latitude co-ordinate systems (Chisham, 2017; Kilcommons et al., 2017; Redmon et al., 2010; Zhu et al., 2020), where measurements are organized in spatial bins that adapt relative to the boundaries in question. However, this analysis is only possible if boundary location estimates for the measurement epoch are available. This is not the case for the whole interval of data presented here.

Another source of mixture distributions is the ionospheric asymmetries introduced by changes in IMF B_Y. Variations in IMF B_Y result in variations in the MLT extents of the R1 and R2 FAC and vorticity regions, and hence have similar mixing effects to the expanding-contracting polar cap when combining data on fixed coordinate grids. The spatial variations of average vorticity for different IMF orientations were presented in Chisham et al. (2009). These show that while the patterns of vorticity around dawn and dusk are similar regardless of the IMF orientation, those around noon and midnight vary significantly, where the MLT of the switch between the dominant vorticity directions depends heavily on the IMF orientation. In this study, we have combined all vorticity measurements made at each location, regardless of the IMF orientation. This will result in mixture distributions in the measured PDFs close to noon and midnight.

In future work, we intend to separate the vorticity data by IMF direction (as in Chisham et al., 2009) to see if this addresses this problem. However, the consequent reduced data in the PDFs in many of the spatial bins (using the present data set) would increase the uncertainty in the MLE q-exponential fitting. This would be particularly significant at the high and low latitude extents of the field-of-view, where the overall occurrence of vorticity estimates reduces. The estimated values of q and κ in this region are already relatively noisy (see Figure 6) without being subdivided by IMF direction. Consequently, to confidently cover a

similar field-of-view, this proposed analysis would probably require either an increase in the spatial bin size or an extension of the measurement epoch beyond the 2000–2006 year interval.

4.1.2. Measurement Uncertainties

As with all measured quantities, there is a level of uncertainty in the individual vorticity estimates. Hence, the measured PDFs are a convolution of the real PDF at that location with a function that represents the measurement and algorithmic errors and uncertainties. These errors are most likely to result from missing or poor velocity estimates around the closed loops used to determine the vorticity (see Chisham et al., 2009 for full details of the vorticity determination), although they could also result from inaccurate mapping of the SuperDARN measurements (see e.g., Chisham et al., 2008). In the absence of systematic errors, we would expect this error function to be approximately Gaussian due to these random errors, although its width is difficult to estimate without realistic simulations of the measurement process. This convolution will have the effect of increasing the variance of the measured PDFs, although it is unlikely to significantly change their shape.

There is also an effect on the PDFs owing to the different measurement scales of the closed loops formed by the overlapping radar beams. As shown in Figure 1, these loops are larger at greater distances from the radars due to the divergence of the radar beams. Hence, these larger loops are typically at higher latitudes. Studying the variation of the vorticity PDFs with measurement scale (not shown) shows that the PDFs become more kurtotic and narrower as the measurement scale reduces; as the scales increase (beyond the measurement scales used in this study), the PDFs increasingly tend toward a Gaussian. Hence, the probability of measuring large vorticity values will decrease if the measurement scale increases significantly. This may partially explain the higher values of q determined in R2 at the lowest latitudes where the measurement scales are the smallest. However, as there is no obvious monotonic variation of q and κ with latitude, this is only likely to be a minor factor affecting the PDF shape and scale.

4.2. Interpretation of the Model Fit Parameters

In this paper, we have presented a statistical representation of ionospheric vorticity on the smallest measurement scales allowed by SuperDARN and how this statistical representation varies spatially across the northern polar ionosphere. These statistical results show that the large-scale averaged picture of ionospheric vorticity presented by Chisham et al. (2009) represents a gross simplification of the true picture, much like the averaged pictures of FAC structure (Anderson et al., 2008; Edwards et al., 2020; Weimer, 2001, 2005). The PDFs show that the measured vorticity value at any location can be vastly different from the average value, often in the different sense, and often significantly larger than the average. Hence, a similar picture would be expected for FACs. The occurrence of these larger values will become more probable as the measurement scale decreases.

Increased FAC structure has been shown to exist on small scales (Lühr et al., 1994; Neubert & Christiansen, 2003; Rother et al., 2007) with extreme FAC values increasing with decreasing scale size. Similarly, we would expect increased vorticity structure on smaller scales with the magnitude and probability of extreme vorticity values increasing with decreasing scale size. In this study, the measurement scale is restricted by the SuperDARN instrumental setup, and so it is not possible to measure vorticity on the smallest scales, below ~100 km. However, the statistical analysis presented here has helped to better understand how the large-scale averaged picture of vorticity emerges from the aggregation of smaller scale vorticity measurements. It is likely that FACs can be understood in a similar way.

We have shown that the measured PDFs of ionospheric vorticity fluctuations are well modeled by q-exponential probability distributions at all locations in the polar ionosphere. These distributions have previously been shown to successfully model fluctuations in other space plasma measurements (e.g., Barbosa et al., 2017; Burlaga et al., 2007; Esquivel & Lazarian, 2010). The parameter q is associated with the level of kurtosis in the distribution, and hence, the amount of turbulent intermittency. Higher values of q reflect more leptokurtic tails and hence increasing intermittency (see Figure 2). The value of κ is associated with the variance in the distribution, and hence, how much the vorticity varies from the typical magnitude of the rotational plasma flow.

Based on the results discussed in Section 3.3 and shown in Figure 6, we find that vorticities in the average R2 current region below 70° latitude are generally relatively weak (low κ) but intermittent (high q). This also suggests that the current systems are more fragmented and filamentary in R2, resulting in an increase in the small-scale structure, such as seen in parts of the auroral zone. As the R2 FACs connect to the partial ring current, this is likely to be the source of this turbulence.

Weak and intermittent vorticity is also seen in the open field line region poleward of the R1 current region, that is, poleward of 80° on the dayside and poleward of 75° on the nightside. This open field line intermittency is slightly less than that in the R2 region and more spatially structured, suggesting that it has a different physical cause. Abel et al. (2007, 2009) showed that in the nightside open field line region moments of velocity gradients in plasma flow (i.e., structure functions) were consistent with the so-called p model of intermittent Kraichnan-Iroshnikov (i.e., 2-D) turbulence. They argued that the intermittency was inherited from that of the solar wind because both ionospheric and solar wind turbulence could be described by a p model with a similar value for the intermittency parameter p, and also because the intermittency disappeared during northward IMF when ionospheric flows would be decoupled from the solar wind. Thus, we propose the same cause for the intermittency seen here in open field line vorticity.

In contrast to the open field line and R2 regions, vorticities are typically stronger but less intermittent in the average R1 current region between 70° and 80° latitude on the dayside and between 70° and 75° on the nightside. However, there are distinct differences between the PDFs on the dayside and nightside.

On the dayside, the R1 vorticities are strongest but the least intermittent, even though we would expect them to be directly driven by the solar wind like in the open field line region. To explain this, we speculate that intermittency may be reduced by the relatively high and homogeneous conductance from solar illumination in the dayside R1 region compared to the open field line region.

On the nightside, the R1 currents connect to the magnetotail current sheet and are driven by substorms and nightside reconnection, which are indirectly driven by the solar wind. Thus, here, a difference in vorticity to that in the directly driven open field line region is understandable. The simplest large-scale picture of substorms depicts FACs at either end of a westward electrojet, forming the substorm current wedge (SCW). However, the real situation is more complex, with significant small-scale structure being observed within the traditional large-scale SCW (Murphy et al., 2013). Forsyth et al. (2014) have shown that the SCW comprises lots of filamentary current sheets and substructure on scales of 100 km, some of which are oppositely directed to the larger scale current. These small-scale filamentary current sheets seen during substorms suggest that the nightside R1 vorticities are typically more intermittent than those observed on the dayside. The larger values of q determined for the nightside R1 PDFs support this interpretation.

4.3. Regarding the Measurement of the Probability of Extreme FACs

The interpretation of the character of the vorticity PDFs above has focused heavily on the role of FACs. Given the intimate connection between vorticity and FACs, we might also expect distributions of FAC to have similar leptokurtic and heavy-tailed forms. However, although small-scale measurements of extreme FACs have been made, the distribution of all FAC fluctuations and the probability of extreme values in different ionospheric regions has not been studied. A long-tailed distribution of "intense kilometer-scale" FAC densities has been reported (Rother et al., 2007), but this was of peak currents during an "event," and not of all the FAC measurements. No attempt was made to model this distribution or to assess whether it was leptokurtic or heavy-tailed.

To fully understand FACs and the relationship between measurements on different scales, a similar statistical analysis to that of vorticity presented here, is required. Given the close relationship of FACs with vorticity, one question is whether it is possible to estimate the equivalent PDFs of FAC fluctuations directly from the PDFs of vorticity. The connection between FAC and vorticity in the ionosphere can be expressed in terms of the $\mathbf{E} \times \mathbf{B}$ drift velocity $\mathbf{v}$ (Freeman et al., 1990; Sofko et al., 1995) as

$$J_{||} = -\Sigma_P \mathbf{B} \cdot \boldsymbol{\omega} - (\mathbf{v} \times \mathbf{B}) \cdot \nabla \Sigma_P - |\mathbf{B}| \, \mathbf{v} \cdot \nabla \Sigma_H \tag{5}$$

where $\omega = \nabla \times \mathbf{v}$ is the ionospheric flow vorticity. Hence, in the limit of constant (fixed Σ_P) and uniform ionospheric conductance ($\nabla\Sigma_P = \nabla\Sigma_H = 0$), the FAC distributions should match those of vorticity. However, such conditions are generally limited to the sunlit region of the ionosphere.

Equation 5 implies that extreme FACs are not solely associated with regions of extreme vorticity, but also with regions where extreme spatial gradients in the Hall or Pedersen conductance exist, as might occur at the poleward and equatorward boundaries of the auroral zones. These gradients in conductance are difficult to measure over large areas with present instrumentation. Hence, the production of statistical distributions of these gradients is not presently feasible. This may change with the advent of new instrumentation, such as the upcoming EISCAT 3D system (McCrea et al., 2015).

The alternative is to determine PDFs of FACs, and hence the probability of extreme FACs, independent of vorticity measurements, using direct FAC measurements. The only data set large enough to allow the production of reliable PDFs across the whole polar ionosphere would be that from Active Magnetosphere and Planetary Electrodynamics Response Experiment (AMPERE) (Anderson et al., 2014; Coxon et al., 2018). The AMPERE data set consists of FACs at a 10-min cadence, determined by combining magnetic field fluctuations from the constellation of Iridium spacecraft. Many years of AMPERE FAC observations are now available that would enable the direct estimation of PDFs of FAC using a similar analysis to that used to analyze the SuperDARN vorticity data. These would be on a similar measurement scale to the SuperDARN vorticity measurements. However, additional challenges may exist owing to the spatial averaging and limited temporal resolution of the AMPERE measurements.

5. Summary and Conclusions

The statistical study of ionospheric vorticity presented here helps to understand the connections between flow turbulence, vorticity, and FACs in the polar ionosphere, and the different effects of the drivers of these processes.

From the analysis presented in this study, we can make the following conclusions:

1. The observed systematic spatial variation of the q-exponential fit parameters across the northern hemisphere polar ionosphere shows that the variations in vorticity are organized similar to the different FAC systems.
2. The vorticity PDFs show that at any location a much wider range of values are observed, of both senses of vorticity, that cannot be easily predicted from the local average value.
3. Modeling of the observed vorticity PDFs allows us to understand differences between the R1 and R2 regions. Although the vorticity has greater variance in R1, vorticity is more intermittent in R2, meaning that extreme flows are more likely there.
4. Extreme values of vorticity (and by association, of field-aligned current), are observed with a nonnegligible probability in most regions of the polar ionosphere and hence, likely have a disproportionate effect on M-I coupling processes.

Data Availability Statement

The raw SuperDARN data are freely available from the BAS SuperDARN data mirror (https://www.bas.ac.uk/project/superdarn). The SuperDARN vorticity data products used in this paper are freely available—Chisham (2020), https://doi.org/10.5285/F0149848-BD81-4A3E-AC20-67D347E7D480.

References

Abel, G. A., Freeman, M. P., & Chisham, G. (2006). Spatial structure of ionospheric convection velocities in regions of open and closed magnetic field topology. *Geophysical Research Letters*, *33*, L24103. https://doi.org/10.1029/2006GL027919

Abel, G. A., Freeman, M. P., & Chisham, G. (2009). IMF clock angle control of multifractality in ionospheric velocity fluctuations. *Geophysical Research Letters*, *36*, L19102. https://doi.org/10.1029/2009GL040336

Abel, G. A., Freeman, M. P., Chisham, G., & Watkins, N. W. (2007). Investigating turbulent structure of ionospheric plasma velocity using the Halley SuperDARN radar. *Nonlinear Processes in Geophysics*, *14*, 799–809. https://doi.org/10.5194/npg-14-799-2007

Anderson, B. J., Korth, H., Waters, C. L., Green, D. L., Merkin, V. G., Barnes, R. J., & Dyrud, L. P. (2014). Development of large-scale Birkeland currents determined from Active Magnetosphere and Planetary Electrodynamics Response Experiment. *Geophysical Research Letters*, *41*, 3017–3025. https://doi.org/10.1002/2014gl059941

Anderson, B. J., Korth, H., Waters, C. L., Green, D. L., & Stauning, P. (2008). Statistical Birkeland current distributions from magnetic field observations by the Iridium constellation. *Annales Geophysicae*, *26*, 671–687. https://doi.org/10.5194/angeo-26-671-2008

Anselmet, F., Antonia, R. A., & Danaila, L. (2001). Turbulent flows and intermittency in laboratory experiments. *Planetary and Space Science*, *49*, 1177–1191. https://doi.org/10.1016/s0032-0633(01)00059-9

Barbosa, C. S., Caraballo, R., Alves, L. R., Hartmann, G. A., Beggan, C. D., Viljanen, A., et al. (2017). The Tsallis statistical distribution applied to geomagnetically induced currents. *Space Weather*, *15*, 1094–1101. https://doi.org/10.1002/2017SW001631

Boffetta, G., Celani, A., Musacchio, S., & Vergassola, M. (2002). Intermittency in two-dimensional Ekham-Navier-Stokes turbulence. *Physical Review E - Statistical Physics, Plasmas, Fluids, and Related Interdisciplinary Topics*, *66*, 026304. https://doi.org/10.1103/PhysRevE.66.026304

Burlaga, L. F., Vinas, A. F., & Wang, C. (2007). Tsallis distributions of magnetic field strength variations in the heliosphere: 5 to 90 AU. *Journal of Geophysical Research*, *112*, A07206. https://doi.org/10.1029/2006JA012213

Chaston, C. C., Salem, C., Bonnell, J. W., Carlson, C. W., Ergun, R. E., Strangeway, R. J., & McFadden, J. P. (2008). The turbulent Alfvénic aurora. *Physical Review Letters*, *100*, 175003. https://doi.org/10.1103/physrevlett.100.175003

Chaston, C. C., Seki, K., Sakanoi, T., Asamura, K., & Hirahara, M. (2010). Motion of aurorae. *Geophysical Research Letters*, *37*, L08104. https://doi.org/10.1029/2009GL042117

Chaston, C. C., Seki, K., Sakanoi, T., Asamura, K., Hirahara, M., & Carlson, C. W. (2011). Cross-scale coupling in the auroral acceleration region. *Geophysical Research Letters*, *38*, L20101. https://doi.org/10.1029/2011GL049185

Chisham, G. (2017). A new methodology for the development of high-latitude ionospheric climatologies and empirical models. *Journal of Geophysical Research*, *122*, 932–947. https://doi.org/10.1002/2016JA023235

Chisham, G. (2020). *Ionospheric vorticity across the northern polar ionosphere determined from SuperDARN velocity data - 2000 to 2005 inclusive [Data set]*. UK Polar Data Centre, Natural Environment Research Council, UK Research & Innovation. https://doi.org/10.5285/F0149848-BD81-4A3E-AC20-67D347E7D480

Chisham, G., & Freeman, M. P. (2010). On the non-Gaussian nature of ionospheric vorticity. *Geophysical Research Letters*, *37*, L12103. https://doi.org/10.1029/2010GL043714

Chisham, G., Freeman, M. P., Abel, G. A., Bristow, W. A., Marchaudon, A., Ruohoniemi, J. M., & Sofko, G. J. (2009). Spatial distribution of average vorticity in the high-latitude ionosphere and its variation with interplanetary magnetic field direction and season. *Journal of Geophysical Research*, *114*, A09301. https://doi.org/10.1029/2009JA014263

Chisham, G., Lester, M., Milan, S. E., Freeman, M. P., Bristow, W. A., Grocott, A., et al. (2007). A decade of the Super Dual Auroral Radar Network (SuperDARN): Scientific achievements, new techniques and future directions. *Surveys in Geophysics*, *28*, 33–109. https://doi.org/10.1007/s10712-007-9017-8

Chisham, G., Yeoman, T. K., & Sofko, G. J. (2008). Mapping ionospheric backscatter measured by the SuperDARN HF radars - Part 1: A new empirical virtual height model. *Annales Geophysicae*, *26*, 823–841. https://doi.org/10.5194/angeo-26-823-2008

Clausen, L. B. N., Baker, J. B. H., Ruohoniemi, J. M., Milan, S. E., & Anderson, B. J. (2012). Dynamics of the region 1 Birkeland current oval derived from the Active Magnetosphere and Planetary Electrodynamics Response Experiment (AMPERE). *Journal of Geophysical Research*, *117*, A06233. https://doi.org/10.1029/2012ja017666

Clausen, L. B. N., Baker, J. B. H., Ruohoniemi, J. M., Milan, S. E., Coxon, J. C., Wing, S., et al. (2013). Temporal and spatial dynamics of the regions 1 and 2 Birkeland currents during substorms. *Journal of Geophysical Research*, *118*, 3007–3016. https://doi.org/10.1002/jgra.50288

Cowley, S. W. H. (2000). Magnetosphere-Ionosphere interactions: A tutorial review. In S. Ohtani, R. Fujii, M. Hesse, & R. L. Lysak (Eds.), *Magnetospheric current systems, geophysical monograph 118* (pp. 91–106). AGU. https://doi.org/10.1029/gm118p0091

Cowley, S. W. H., & Lockwood, M. (1992). Excitation and decay of solar wind-driven flows in the magnetosphere-ionosphere system. *Annales Geophysicae*, *10*, 103–115.

Coxon, J. C., Milan, S. E., & Anderson, B. J. (2018). A review of birkeland current research using AMPERE. In A. Keiling, O. Marghitu, & M. Wheatland (Eds.), *Electric currents in geospace and beyond, geophysical monograph 235* (pp. 259–278). American Geophysical Union. https://doi.org/10.1002/9781119324522.ch16

Coxon, J. C., Milan, S. E., Clausen, L. B. N., Anderson, B. J., & Korth, H. (2014). A superposed epoch analysis of the regions 1 and 2 Birkeland currents observed by AMPERE during substorms. *Journal of Geophysical Research*, *119*, 9834–9846. https://doi.org/10.1002/2014ja020500

Dungey, J. W. (1961). Interplanetary magnetic field and the auroral zones. *Physical Review Letters*, *6*, 47. https://doi.org/10.1103/physrevlett.6.47

Edwards, T. R., Weimer, D. R., Olsen, N., Lühr, H., Tobiska, W. K., & Anderson, B. J. (2020). A third generation field-aligned current model. *Journal of Geophysical Research*, *125*, e2019JA027249. https://doi.org/10.1029/2019JA027249

Erlandson, R. E., Zanetti, L. J., Potemra, T. A., Bythrow, P. F., & Lundin, R. (1988). IMF *By* dependence of region 1 Birkeland currents near noon. *Journal of Geophysical Research*, *93*, 9804–9814. https://doi.org/10.1029/ja093ia09p09804

Esquivel, A., & Lazarian, A. (2010). Tsallis statistics as a tool for studying interstellar turbulence. *The Astrophysical Journal*, *710*, 125–132. https://doi.org/10.1088/0004-637x/710/1/125

Forsyth, C., Fazakerley, A. N., Rae, I. J., Watt, C. E. J., Murphy, K., Wild, J. A., et al. (2014). In situ spatiotemporal measurements of the detailed azimuthal substructure of the substorm current wedge. *Journal of Geophysical Research*, *119*, 927–946. https://doi.org/10.1002/2013ja019302

Freeman, M. P., Forsyth, C., & Rae, I. J. (2019). The influence of substorms on extreme rates of change of the surface horizontal magnetic field in the United Kingdom. *Space Weather*, *17*, 827–844. https://doi.org/10.1029/2018SW002148

Freeman, M. P., Southwood, D. J., Lester, M., & Waldock, J. A. (1990). Measurement of field-aligned currents by the SABRE coherent scatter radar. In C. T. Russell, E. R. Priest, & L. C. Lee (Eds.), *Physics of magnetic flux ropes, geophysical monograph series, 58* (pp. 575–580). American Geophysical Union. https://doi.org/10.1029/gm058p0575

Greenwald, R. A., Baker, K. B., Dudeney, J. R., Pinnock, M., Jones, T. B., Thomas, E. C., et al. (1995). DARN/SuperDARN: A global view of the dynamics of high-latitude convection. *Space Science Reviews*, *71*, 761–796. https://doi.org/10.1007/bf00751350

Hasegawa, A., & Sato, T. (1979). Generation of field-aligned current during substorm. In S. I. Akasofu, D. Reidel, & Hingham (Eds.), *Dynamics of the magnetosphere*. https://doi.org/10.1007/978-94-009-9519-2_28

Hughes, C. W., Thompson, A. F., & Wilson, C. (2010). Identification of jets and mixing barriers from sea level and vorticity measurements using simple statistics. *Ocean Modelling*, *32*, 44–57. https://doi.org/10.1016/j.ocemod.2009.10.004

Iijima, T., & Potemra, T. A. (1976a). The amplitude distribution of field-aligned currents at northern high latitudes observed by Triad. *Journal of Geophysical Research*, *81*, 2165–2174. https://doi.org/10.1029/ja081i013p02165

Iijima, T., & Potemra, T. A. (1976b). Field-aligned currents in the dayside cusp observed by Triad. *Journal of Geophysical Research*, *81*, 5971–5979. https://doi.org/10.1029/ja081i034p05971

Kilcommons, L. M., Redmon, R. J., & J Knipp, D. (2017). A new DMSP magnetometer and auroral boundary data set and estimates of field-aligned currents in dynamic auroral boundary coordinates. *Journal of Geophysical Research*, *122*, 9068–9079. https://doi.org/10.1002/2016JA023342

Kintner, P. M., & Seyler, C. E. (1985). The status of observations and theory of high latitude ionospheric and magnetospheric plasma turbulence. *Space Science Reviews*, *41*, 91–129. https://doi.org/10.1007/bf00241347

Lockwood, M., Cowley, S. W. H., & Freeman, M. P. (1990). The excitation of plasma convection in the high-latitude ionosphere. *Journal of Geophysical Research*, *95*, 7961–7972. https://doi.org/10.1029/ja095ia06p07961

Lühr, H., Warnecke, J., Zanetti, L. J., Lindqvist, P. A., & Hughes, T. J. (1994). Fine structure of field-aligned current sheets deduced from spacecraft and ground-based observations: Initial FREJA results. *Geophysical Research Letters*, *21*, 1883–1886. https://doi.org/10.1029/94gl01278

McCrea, I., Aikio, A., Alfonsi, L., Belova, E., Buchert, S., Clilverd, M., et al. (2015). The science case for the EISCAT_3D radar. *Progress in Earth and Planetary Science*, *2*, 21. https://doi.org/10.1186/s40645-015-0051-8

Murphy, K. R., Mann, I. R., Rae, I. J., Waters, C. L., Frey, H. U., Kale, A., et al. (2013). The detailed spatial structure of field aligned currents comprising the substorm current wedge. *Journal of Geophysical Research*, *118*, 7714–7727. https://doi.org/10.1002/2013JA018979

Neubert, T., & Christiansen, F. (2003). Small-scale, field-aligned currents at the top-side ionosphere. *Geophysical Research Letters*, *30*(19), 2010. https://doi.org/10.1029/2003GL017808

Nishitani, N., Ruohoniemi, J. M., Lester, M., Baker, J. B. H., Koustov, A. V., Shepherd, S. G., et al. (2019). Review of the accomplishments of mid-latitude Super Dual Auroral Radar Network (SuperDARN) HF radars. *Progress in Earth and Planetary Science*, *6*, 27. https://doi.org/10.1186/s40645-019-0270-5

Pasquero, C., & Falkovich, G. (2002). Stationary spectrum of vorticity cascade in two-dimensional turbulence. *Physical Review E - Statistical Physics, Plasmas, Fluids, and Related Interdisciplinary Topics*, *65*, 056305. https://doi.org/10.1103/physreve.65.056305

Picoli, S., Jr., Mendes, R. S., Malacarne, L. C., & Santos, R. P. B. (2009). q-distributions in complex systems: A brief review. *Brazilian Journal of Physics*, *39*, 468–474. https://doi.org/10.1590/s0103-97332009000400023

Redmon, R. J., Peterson, W. K., Andersson, L., Kihn, E. A., Denig, W. F., Hairston, M., & Coley, R. (2010). Vertical thermal O+ flows at 850 km in dynamic auroral boundary coordinates. *Journal of Geophysical Research*, *115*, A00J08. https://doi.org/10.1029/2010JA015589

Rother, M., Schlegel, K., & Lühr, H. (2007). CHAMP observation of intense kilometer-scale field-aligned currents, evidence for an ionospheric Alfvén resonator. *Annales Geophysicae*, *25*, 1603–1615. https://doi.org/10.5194/angeo-25-1603-2007

Sardeshmukh, P. D., & Sura, P. (2009). Reconciling non-Gaussian climate statistics with linear dynamics. *Journal of Climate*, *22*, 1193–1207. https://doi.org/10.1175/2008jcli2358.1

Shalizi, C. R. (2007). *Maximum likelihood estimation for q-exponential (Tsallis) distributions*. arXiv:math/0701854v2.

Sofko, G. J., Greenwald, R. A., & Bristow, W. (1995). Direct determination of large-scale magnetospheric field-aligned currents with Super-DARN. *Geophysical Research Letters*, *22*, 2041–2044. https://doi.org/10.1029/95gl01317

Stern, D. P. (1983). The origins of Birkeland currents. *Reviews of Geophysics*, *21*, 125–138. https://doi.org/10.1029/rg021i001p00125

Tsallis, C. (2009). *Introduction to nonextensive statistical mechanics - Approaching a complex world* (pp. 37–41). Springer.

Vasyliunas, V. M. (1984). Fundamentals of current description. In T. A. Potemra (Ed.), *Magnetospheric currents, geophys. monogr. ser.* (Vol. 28, p. 63). AGU. https://doi.org/10.1029/gm028p0063

Weimer, D. R. (2001). Maps of ionospheric field-aligned currents as a function of the interplanetary magnetic field derived from Dynamics Explorer 2 data. *Journal of Geophysical Research*, *106*, 12,889–12,902. https://doi.org/10.1029/2000ja000295

Weimer, D. R. (2005). Improved ionospheric electrodynamic models and application to calculating Joule heating rates. *Journal of Geophysical Research*, *110*, A05306. https://doi.org/10.1029/2004JA010884

Wilczek, M., & Friedrich, R. (2009). Dynamical origins for non-Gaussian vorticity distributions in turbulent flows. *Physical Review E - Statistical Physics, Plasmas, Fluids, and Related Interdisciplinary Topics*, *80*, 0016316. https://doi.org/10.1103/physreve.80.016316

Yeoman, T. K., Chisham, G., Baddeley, L. J., Dhillon, R. S., Karhunen, T. J. T., Robinson, T. R., et al. (2008). Mapping ionospheric backscatter measured by the SuperDARN HF radars—Part 2: Assessing SuperDARN virtual height models. *Annales Geophysicae*, *26*, 843–852. https://doi.org/10.5194/angeo-26-843-2008

Zhu, Q., Deng, Y., Richmond, A., Maute, A., Chen, Y.-J., Hairston, M., et al. (2020). Impacts of binning methods on high-latitude electrodynamic forcing: Static versus boundary-oriented binning methods. *Journal of Geophysical Research*, *125*, e2019JA027270. https://doi.org/10.0129/2019JA027270